THE JOURNAL OF PHYSICAL CHEMISTRY C
Article
Cite This: J. Phys. Chem. C 2017, 121, 27351−27356
pubs.acs.org/JPCC

Halide Perovskite Heteroepitaxy: Bond Formation and Carrier Confinement at the PbS−$CsPbBr_3$ Interface

Young-Kwang Jung,[†] Keith T. Butler,[‡] and Aron Walsh*,[†,§]

[†]Department of Materials Science and Engineering, Yonsei University, Seoul 03722, Korea
[‡]Department of Chemistry, University of Bath, Claverton Down, Bath BA2 7AY, United Kingdom
[§]Department of Materials, Imperial College London, Exhibition Road, London SW7 2AZ, United Kingdom

Supporting Information

ABSTRACT: Control of the stability, transport, and confinement of charge carriers (electrons and holes) at interfaces is a key requirement to realize robust halide perovskite devices. The PbS−$CsPbBr_3$ interface is atomically matched with low lattice strain, opening the potential for epitaxial growth. We assess the atomic nature of the interface using first-principles density functional theory calculations to identify (1) the thermodynamically stable (100) surface termination of the halide perovskite; (2) the most favorable (100)|(100) contact geometry; (3) the strong interfacial chemical bonding between PbS and $CsPbBr_3$; (4) the type I (straddling) band alignment that enables electron and hole confinement in the lead sulfide layer. The combination of metal halide perovskites and IV−VI semiconductors represents an important platform for probing interfacial chemical processes and realizing new functionality.

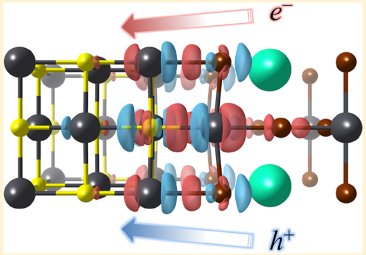

INTRODUCTION

The field of photovoltaics based on halide perovskites as an active layer has developed rapidly.[1−9] This family of materials combines cost efficiency with solution processability and high device performance. Their application domain has recently extended from solar cells to light-emitting diodes,[10] solid-state memory,[11] sensors,[12] and batteries.[13,14] For practical devices, control of the stability, transport, and confinement of charge carriers (e^- and h^+) at interfaces is a key requirement.

In semiconductor devices, interfaces between materials are responsible for injecting or blocking charge carriers. Recombination due to structural defects or interfacial electronic states represents a loss mechanism for device performance. Density functional theory (DFT) has been widely applied to gain important microscopic information about the interfaces of materials.[15] In several contexts, such as semiconductor heterostructures,[16] metal−semiconductor interfaces,[17] and oxide−oxide interfaces,[18] materials modeling has provided important insights about interfacial electronic and structural properties.

For halide perovskites, interfaces with mesoporous metal oxides and organic semiconductors are most common and are poorly defined with chemical disorder and carrier trapping.[19,20] The realization of high-quality pervoskite heterojunctions would enable better characterization and alternative device architectures. This requires epitaxial structure control and band offset engineering. A "dots-in-a-matrix" approach has been applied to disperse lead sulfide quantum dots in a $CH_3NH_3PbI_3$ host,[21] combining the transport properties of halide perovskites and optical emission of PbS quantum dots. However, the lattice mismatch between PbS and $CH_3NH_3PbI_3$ is large (around 5%). To realize the potential of heterostructure architectures, lattice and electronically matched materials combinations are required.[22]

In this work, we probe the chemical and physical properties of the PbS−$CsPbBr_3$ interface, where epitaxial growth is possible because of their similar lattice constants. First, we assess bulk and surface properties of the individual materials to construct reliable interface models based on first-principles electronic structure methods. We then identify the mechanisms by which the interface is stabilized. Finally, we predict the band alignment of PbS and $CsPbBr_3$ as a function of layer thickness of heterostructure, demonstrating the possibility of offset engineering through control of film thickness.

COMPUTATIONAL METHODS

All total energy and electronic structure calculations were performed using Kohn−Sham density functional theory (DFT)[23] within periodic boundary conditions. Projector augmented wave (PAW)[24,25] pseudopotentials as implemented in the Vienna Ab initio Simulation Package (VASP)[26,27] were used, where the plane-wave kinetic cutoff energy is set to 700 eV and the valence states of Pb, S, Cs, and Br are treated explicitly by 14($5d^{10}6s^26p^2$), 6($3s^23p^4$), 9($5s^25p^66s^1$), and 7($4s^24p^5$) electrons, respectively. For atomic structure calculations, the Perdew−Burke−Ernzerhof exchange-correlation functional revised for solids (PBEsol)[28] was employed with convergence criteria of 10^{-5} eV and 10^{-4} eVÅ^{-1} for total energy and forces on the unit cell.

Received: October 9, 2017
Revised: November 15, 2017
Published: November 15, 2017

DOI: 10.1021/acs.jpcc.7b10000
J. Phys. Chem. C 2017, 121, 27351−27356

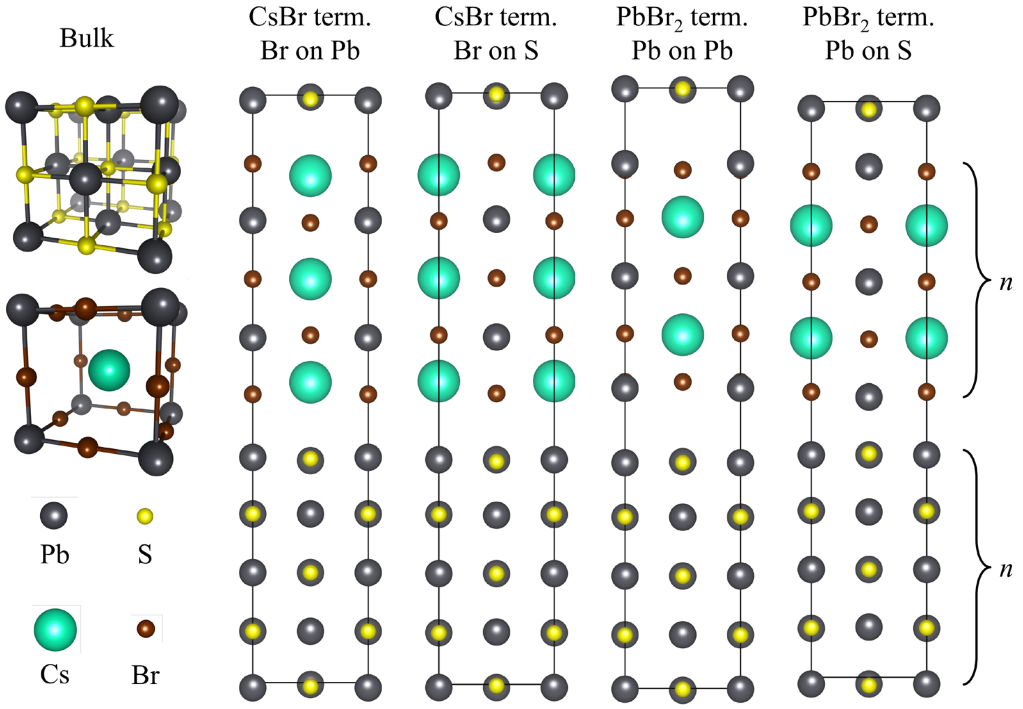

Figure 1. Atomic structures of PbS and $CsPbBr_3$ bulk (in perspective view) and four interface models (in side view) with different contact geometries. "CsBr term" or "$PbBr_2$ term" refers to termination of the $CsPbBr_3(100)$ surface in contact with the PbS(100) surface. "X on Y" (where X = Br or Pb of $CsPbBr_3$ and Y = Pb or S of PbS) explains the atomic configuration at the contact region. The thickness of both materials is determined by n atomic layers. Pb, S, Cs, and Br atoms are represented as black, yellow, green, and brown colored spheres, respectively.

For calculations of the absolute electron energy, a nonlocal hybrid functional (HSE06)[29,30] with spin−orbit coupling (SOC) was used with PBEsol optimized atomic structures. Forty-three percent exchange was adopted for all HSE06 + SOC calculations. For bulk calculations, primitive cells of PbS and $CsPbBr_3$ were considered with Γ-centered k-point grids of 10 × 10 × 10 and 6 × 6 × 6.

For surface calculations, symmetric slab models for three low index surfaces, that is, (100), (110), and (111), were considered with vacuum region of 15 Å, and Γ-centered k-point grids of 9 × 9 × 1, 9 × 6 × 1, 5 × 5 × 1, 6 × 6 × 1, 6 × 4 × 1 and 5 × 5 × 1 were applied for PbS(100), PbS(110), PbS(111), $CsPbBr_3(100)$, $CsPbBr_3(110)$, and $CsPbBr_3(111)$ surfaces, respectively. Geometric optimization of the slabs was performed by allowing full atomic relaxation, while the innermost three atomic layers were fixed at their bulk values. Detailed information on surface slab models is included as Supporting Information. For interface calculations, sandwich-type slab models without vacuum region were considered with Γ-centered k-point grids of 6 × 6 × 3, 6 × 6 × 2, and 6 × 6 × 1 depending on the thickness of the slabs. Constrained relaxation was allowed with the a- and b-axes of the interface unit cell held fixed. The MacroDensity package[31,32] was used to analyze the charge density and local potential of the surfaces and interfaces.

RESULTS AND DISCUSSION

Crystal structures of (rocksalt) PbS and (perovskite) $CsPbBr_3$ in cubic symmetry are shown in Figure 1. The calculated bulk parameters of a_0 = 5.90 (5.87) Å for PbS ($CsPbBr_3$) agree with previous reports.[33,34] The lattice mismatch is predicted to be 0.5%, which ensures low lattice strain when they form an epitaxial interface. The bulk moduli of B_0 = 59.4 (21.5) GPa for PbS ($CsPbBr_3$) were obtained from fitting to the third-order Birch−Murnaghan equation-of-state.[35] PbS has a bulk modulus almost 3 times that of $CsPbBr_3$, which suggests that $CsPbBr_3$ will follow a_0 of PbS at an epitaxial interface. Furthermore, this suggests growth of $CsPbBr_3$ on a PbS substrate as a route to templating formation of a cubic perovskite phase.

To determine the interface orientation, we first calculated the surface energy (E_{surf}) of PbS and $CsPbBr_3$. A facet with low surface energy is more likely to be exposed and, consequentially, more likely to form an interface. Three low index facets of PbS and $CsPbBr_3$ were considered including all possible atomistic terminations. For instance, there are two different terminations for $CsPbBr_3(100)$ facet, CsBr and $PbBr_2$ termination, which are notated as $CsPbBr_3(100)$:CsBr and $CsPbBr_3(100)$:$PbBr_2$ here. Detailed information for surface slab models can be found in Figures S1 and S2.

The surface energy (E_{surf}) was calculated on the basis of the bond cleaving and surface relaxation approach[36,37] following

$$E_{surf}(t) = E_{cl} + E_{rel}(t) \tag{1}$$

where E_{cl} is bond-cleaving energy and $E_{rel}(t)$ is surface-relaxation energy of a slab with t termination. A detailed explanation for E_{cl} and E_{rel} can be found in Supporting Information. The energy of nonstoichiometric surfaces is often calculated as a function of the chemical potential of constituent elements. We used a surface bond cleaving and relaxation approach to directly compare the order of surface energies from different orientations and terminations. All calculated results are tabulated in Table 1. By definition, surfaces with two different chemical terminations in the same orientation require equal energy to cleave bonds, but different relaxation behavior leads to distinct surface energy. According to calculated surface energies, (100) facets show the lowest surface energy among

DOI: 10.1021/acs.jpcc.7b10000
J. Phys. Chem. C 2017, 121, 27351−27356

Table 1. Calculated Bond Cleavage Energy (E_{cl}), Surface-Relaxation Energy (E_{rel}), and Surface Energy (E_{surf}) of Low-Index Facets of PbS and $CsPbBr_3$

(meV/Å^2)	E_{cl}	E_{rel}	E_{surf}
PbS(100)	20.03	−3.94	16.09
PbS(110)	39.42	−9.47	29.96
PbS(111):Pb	89.24	−3.76	85.48
PbS(111):S	89.24	−28.04	61.19
$CsPbBr_3$(100):CsBr	10.76	−5.22	5.54
$CsPbBr_3$(100):$PbBr_2$	10.76	−3.15	7.61
$CsPbBr_3$(110):CsPbBr	43.79	−8.30	35.49
$CsPbBr_3$(110):Br_2	43.79	−10.22	33.57
$CsPbBr_3$(111):$CsBr_3$	36.41	−7.50	28.91
$CsPbBr_3$(111):Pb	36.41	−5.59	30.82

the low index facets for both PbS and $CsPbBr_3$. Therefore, we constructed interface slab models along (100) orientation.

When heterointerfaces between different structures are formed, crystal chemistry plays a critical role in determining structure and function.[38] To study the interface, four slab models with different atomic configurations were constructed (see Figure 1) on the basis of the values from our bulk and surface calculations (i.e., a_0 of PbS and (100) orientation). These four models account for all possible combinations of termination and local arrangement of the atoms on either side of the interface. To find the most favorable contact geometry, the interface energy (E_{intf}) was calculated following

$$E_{\mathrm{intf}} = \frac{1}{2A}[E_{\mathrm{slab}}^{\mathrm{interface}} - E_{\mathrm{slab}}^{\mathrm{PbS}} - E_{\mathrm{slab}}^{\mathrm{CsPbBr_3}}] \tag{2}$$

where A is interface (surface) area; $E_{\mathrm{slab}}^{\mathrm{interface}}$, $E_{\mathrm{slab}}^{\mathrm{PbS}}$, and $E_{\mathrm{slab}}^{\mathrm{CsPbBr_3}}$ are the DFT total energies from the PbS−$CsPbBr_3$ interface, PbS, and $CsPbBr_3$ slab calculations. For the slab calculations to obtain $E_{\mathrm{slab}}^{\mathrm{PbS}}$ and $E_{\mathrm{slab}}^{\mathrm{CsPbBr_3}}$, internal coordinates of atoms were fully relaxed while unit cell vectors were constrained so that all slabs have the same A. The consideration of sandwich-type interface slab models (i.e., two identical interfaces in one unit cell) necessitates a factor of 1/2. Interface energies as a function of contact geometry and the number of atomic layers (n) of the interface slab are shown in Figure 2a and are tabulated in Table S1. Among the four interface models, the $PbBr_2$ termination Pb on S model has the lowest interface energy. Interestingly, the interlayer distance between PbS and $CsPbBr_3$ follows the same order as interface energy (i.e., $PbBr_2$ termination Pb on S model has the shortest interlayer distance, while $PbBr_2$ termination Pb on Pb model has the longest interlayer distance).

To understand the origin of the interface stability, we pictured the electron density redistribution along the interface (see Figure 3) by calculating charge density difference ($\Delta\rho$) as

$$\Delta\rho = \rho_{\mathrm{slab}}^{\mathrm{interface}} - \rho_{\mathrm{slab}}^{\mathrm{PbS}} - \rho_{\mathrm{slab}}^{\mathrm{CsPbBr_3}} \tag{3}$$

where $\rho_{\mathrm{slab}}^{\mathrm{interface}}$, $\rho_{\mathrm{slab}}^{\mathrm{PbS}}$, and $\rho_{\mathrm{slab}}^{\mathrm{CsPbBr_3}}$ denote electron density from PbS−$CsPbBr_3$ interface, PbS, and $CsPbBr_3$ slab calculations.

At the CsBr terminated Br-on-Pb interface, although a strong interaction (i.e., alternating charge accumulation and depletion region) from the Br−Pb pair is observed, Cs−Pb repulsion (i.e., charge accumulation region only) is strong enough to make this interface less stable. Likewise, at the CsBr termination Br-on-S interface, a weak interaction (i.e., a pair of charge accumulation and depletion region) from Cs−S pair is observed, but because of Br−S repulsion (i.e., charge depletion region only), it is also not stable. In the case of the $PbBr_2$ terminated Pb-on-Pb interface, strong Pb−Pb repulsion makes it unstable. Among the four models in Figure 3, only the $PbBr_2$ termination Pb-on-S interface model shows strong interaction along the entire contact region. This PbS-$CsPbBr_3$ interface is stabilized by Pb−S and Br−Pb bonds and will be the dominant orientation.

Electronic band offsets between the two materials are calculated by considering the change in potential (ΔV), which is influenced by charge redistribution at the interface.[15] The valence band offset (VBO) and conduction band offset (CBO) are obtained following

$$\mathrm{VBO} = \Delta E_{\mathrm{v}} + \Delta V \tag{4}$$

$$\mathrm{CBO} = \Delta E_{\mathrm{c}} + \Delta V \tag{5}$$

where ΔE_{v} and ΔE_{c} are the difference between the relevant valence and conduction band edges in the two materials. To accurately predict the band offsets, it is necessary to use a hybrid DFT approach. We employed a screened-exchange HSE06 functional that incorporates 43% Hartree−Fock exact exchange as adopted in previous studies.[39,40] The influence of functional choice and spin−orbit coupling on charge density

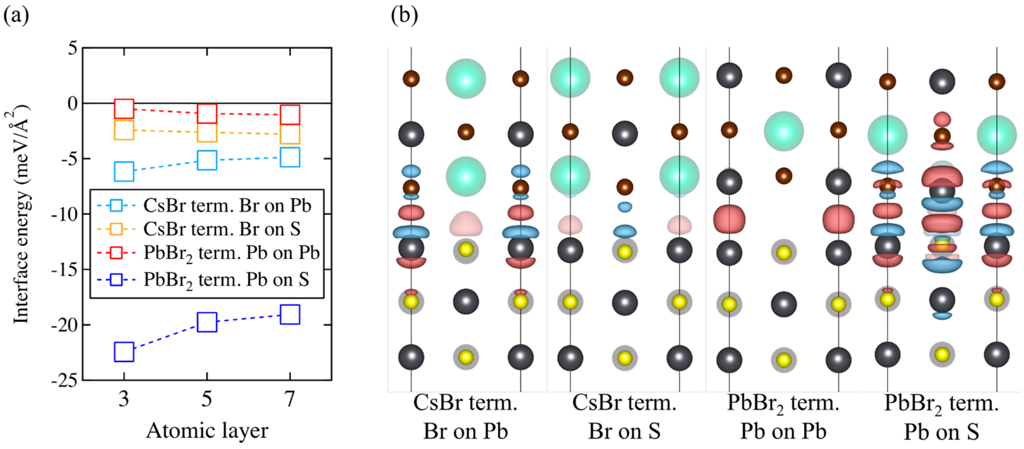

Figure 2. (a) Interface energy of different models as a function of the number of atomic layers and (b) side views of the electronic charge density difference of four interface slab models. The electron density accumulation and depletion regions are indicated in red and black, respectively. For the charge density difference plot, the 5 AL interface models are used, and the isosurface level is set as 0.00675 e/Å^3.

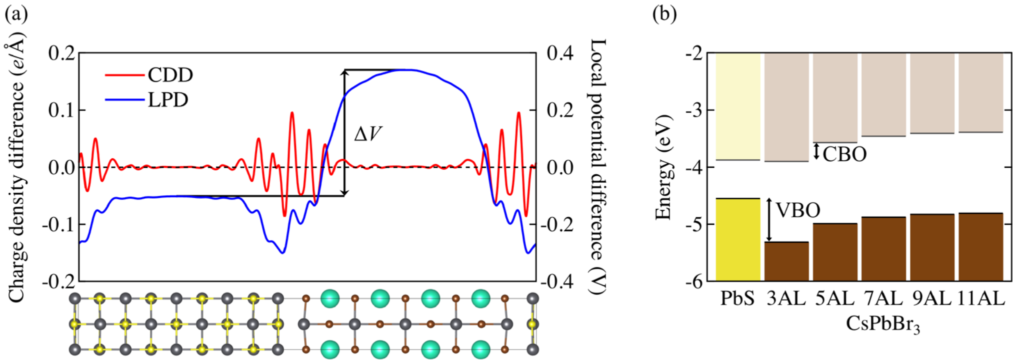

Figure 3. (a) Planar-averaged charge density difference (red line, labeled as CDD) and local potential difference (black line, labeled as LPD). Potential difference (ΔV) is measured between two plateaus at the center of each material. (b) Band alignment between PbS and $CsPbBr_3$ depending on thickness of each layer. The yellow bar indicates the valence band (VB) and conduction band (CB) of PbS and the brown bars indicate those of $CsPbBr_3$.

and electrostatic potential have been tested and are shown in Figure S3.

To understand how local chemical interactions at the interface influence the band alignments, we plot and analyze charge density and potential difference along the interface in Figure 3. The planar-averaged charge density difference shows that the charge redistribution occurs within three atomic layers from the interface while it is negligible at the center region of each material. In response to the charge redistribution, the planar-averaged local potential difference displays a potential gradient at the interface and a plateau in the center regions, where the difference (ΔV) represents the built-in potential which affects the band offset. $CsPbBr_3$ has an increased electrostatic potential upon interface formation because it takes away electron density from PbS. The direction of electron-charge transfer is due to larger electronegativity of Br (2.74) than S (2.44).[41]

The band gaps (E_g) calculated at this level of theory are 0.68 and 1.42 eV for PbS and $CsPbBr_3$, respectively, which are over- and underestimated with respect to experimental band gaps: 0.42 eV for PbS and 2.25 eV for $CsPbBr_3$.[42,43] In part, this is due to the cubic model for $CsPbBr_3$: octahedral distortions (electron−phonon coupling) widen the band gap.[44,45] The calculated band gap of orthorhombic $CsPbBr_3$ is 2.10 eV, which is in better agreement with the measured value of 2.25 eV.[43] This band gap sensitivity demonstrates the potential for tuning the electronic structure of halide perovskites through epitaxial templating and control of structural distortions.[46]

Values of ΔE_v and ΔE_c are calculated to be −0.72 eV and −0.02 eV, which were obtained from the planar-averaged electrostatic potential of PbS(100) and $CsPbBr_3(100){:}PbBr_2$, respectively.[45,47] Further details concerning the method of calculating ΔE_v and ΔE_c can be found in the Supporting Information. In Figure 3b, the band offsets are altered by controlling the thickness of the slab and by changing ΔV as a function of the number of atomic layers (AL). Exact offset values are tabulated in Table S2. As the thickness increases, the built-in potential becomes stronger, which results in a type I band alignment, where both e^- and h^+ will be transferred from $CsPbBr_3$ to PbS and confined in PbS. This kind of type I configuration often results in the stabilization of excitons and is a desirable band alignment for application in devices such as quantum-well light-emitting diodes.

At 3 AL, the interface forms a type II band alignment. The ΔV (consequentially, VBO and CBO as well) shows convergence after 9 AL. The planar-averaged charge density difference and local potential difference plots for 3, 5, 7, 9, and 11 AL are in Figure S4. These results demonstrate how the alignment of the interface can be altered by controlling layer thickness, which is an important consideration when designing potential devices. For extremely thin films and island or wire growth on a substrate, quantum confinement could provide an additional route to tune band energies and emission efficiency.

■ CONCLUSIONS

The lattice mismatch between PbS and $CsPbBr_3$ is less than 1%, which ensures high-quality epitaxy with low strain. Contact along the (100) surface orientation is found to be favorable for both materials following a detailed energetic analysis. The $CsPbBr_3(100){:}PbBr_2$ layer spontaneously grows on the PbS(100) surface by locating Pb on S and Br on Pb with the presence of a strong chemical interaction attributed to heteropolar bond formation. The nature of the heterojunction valence band offset that governs electron and hole carrier distributions and transport at the interface can be altered by changing the thickness of the layers. The PbS−$CsPbBr_3$ interface forms a type I band offset, where e^- and h^+ accumulate in PbS, which could be favorable for light-emitting devices.

■ ASSOCIATED CONTENT

Supporting Information

The Supporting Information is available free of charge on the ACS Publications website at DOI: 10.1021/acs.jpcc.7b10000.

> Additional technical details including convergence tests as well as calculation details on surface energies and valence band offsets.
> (PDF)

■ AUTHOR INFORMATION

Corresponding Author

*E-mail: a.walsh@imperial.ac.uk.

ORCID

Keith T. Butler: 0000-0001-5432-5597
Aron Walsh: 0000-0001-5460-7033

Notes

The authors declare no competing financial interest.

The MacroDensity package used for the band alignment calculations for this article may be accessed at https://github.com/WMD-group/MacroDensity.

■ ACKNOWLEDGMENTS

We thank A. Soon for fruitful discussions. The work at ICL was supported by the EPSRC (Grant No. EP/K016288/1 and EP/M009580/1) and the ERC (Grant No. 277757). A.W. is supported by a Royal Society University Research Fellowship. Via our membership of the U.K.'s HEC Materials Chemistry Consortium, which is funded by EPSRC (EP/L000202), this work used the ARCHER UK National Supercomputing Service (http://www.archer.ac.uk).

■ REFERENCES

(1) Kojima, A.; Teshima, K.; Shirai, Y.; Miyasaka, T. Organometal Halide Perovskites as Visible-Light Sensitizers for Photovoltaic Cells. *J. Am. Chem. Soc.* **2009**, *131*, 6050−6051.

(2) Gao, P.; Grätzel, M.; Nazeeruddin, M. K. Organohalide Lead Perovskites for Photovoltaic Applications. *Energy Environ. Sci.* **2014**, *7*, 2448−2463.

(3) Park, N.-G. Perovskite Solar Cells: An Emerging Photovoltaic Technology. *Mater. Today* **2015**, *18*, 65−72.

(4) Giorgi, G.; Yamashita, K. Organic-Inorganic Halide Perovskites: An Ambipolar Class of Materials With Enhanced Photovoltaic Performances. *J. Mater. Chem. A* **2015**, *3*, 8981−8991.

(5) Zhang, W.; Eperon, G. E.; Snaith, H. J. Metal Halide Perovskites for Energy Applications. *Nat. Energy* **2016**, *1*, 16048.

(6) Sun, Y.-Y.; Shi, J.; Lian, J.; Gao, W.; Agiorgousis, M. L.; Zhang, P.; Zhang, S. Discovering Lead-Free Perovskite Solar Materials With a Split-Anion Approach. *Nanoscale* **2016**, *8*, 6284−6289.

(7) Correa-Baena, J.-P.; Abate, A.; Saliba, M.; Tress, W.; Jesper Jacobsson, T.; Grätzel, M.; Hagfeldt, A. The Rapid Evolution of Highly Efficient Perovskite Solar Cells. *Energy Environ. Sci.* **2017**, *10*, 710−727.

(8) Whalley, L. D.; Frost, J. M.; Jung, Y.-K.; Walsh, A. Perspective: Theory and Simulation of Hybrid Halide Perovskites. *J. Chem. Phys.* **2017**, *146*, 220901.

(9) Yang, W. S.; Park, B.-W.; Jung, E. H.; Jeon, N. J.; Kim, Y. C.; Lee, D. U.; Shin, S. S.; Seo, J.; Kim, E. K.; Noh, J. H.; et al. Iodide Management in Formamidinium-Lead-Halide-based Perovskite Layers for Efficient Solar Cells. *Science* **2017**, *356*, 1376−1379.

(10) Veldhuis, S. A.; Boix, P. P.; Yantara, N.; Li, M.; Sum, T. C.; Mathews, N.; Mhaisalkar, S. G. Perovskite Materials for Light-Emitting Diodes and Lasers. *Adv. Mater.* **2016**, *28*, 6804−6834.

(11) Liu, D.; Lin, Q.; Zang, Z.; Wang, M.; Wangyang, P.; Tang, X.; Zhou, M.; Hu, W. Flexible All-Inorganic Perovskite $CsPbBr_3$ Nonvolatile Memory Device. *ACS Appl. Mater. Interfaces* **2017**, *9*, 6171−6176.

(12) Fang, Y.; Dong, Q.; Shao, Y.; Yuan, Y.; Huang, J. Highly Narrowband Perovskite Single-Crystal Photodetectors Enabled by Surface-Charge Recombination. *Nat. Photonics* **2015**, *9*, 679−686.

(13) Xia, H.-R.; Sun, W.-T.; Peng, L.-M. Hydrothermal Synthesis of Organometal Halide Perovskites for Li-Ion Batteries. *Chem. Commun.* **2015**, *51*, 13787−13790.

(14) Dawson, J. A.; Naylor, A. J.; Eames, C.; Roberts, M.; Zhang, W.; Snaith, H. J.; Bruce, P. G.; Islam, M. S. Mechanisms of Lithium Intercalation and Conversion Processes in Organic-Inorganic Halide Perovskites. *ACS Energy Lett.* **2017**, *2*, 1818−1824.

(15) Peressi, M.; Binggeli, N.; Baldereschi, A. Band Engineering at Interfaces: Theory and Numerical Experiments. *J. Phys. D: Appl. Phys.* **1998**, *31*, 1273−1299.

(16) Kim, C.-E.; Tak, Y.-J.; Butler, K. T.; Walsh, A.; Soon, A. Lattice-Mismatched Heteroepitaxy of IV-VI Thin Films on PbTe(001): An Ab Initio Study. *Phys. Rev. B: Condens. Matter Mater. Phys.* **2015**, *91*, 085307.

(17) Wang, Y.; Yang, R. X.; Quhe, R.; Zhong, H.; Cong, L.; Ye, M.; Ni, Z.; Song, Z.; Yang, J.; Shi, J.; et al. Does P-Type Ohmic Contact Exist in WSe_2-metal Interfaces? *Nanoscale* **2016**, *8*, 1179−1191.

(18) Chen, H.; Kolpak, A. M.; Ismail-Beigi, S. Electronic and Magnetic Properties of $SrTiO_3/LaAlO_3$ Interfaces From First Principles. *Adv. Mater.* **2010**, *22*, 2881−2899.

(19) Mosconi, E.; Ronca, E.; De Angelis, F. First-Principles Investigation of the TiO_2/organohalide Perovskites Interface: The Role of Interfacial Chlorine. *J. Phys. Chem. Lett.* **2014**, *5*, 2619−2625.

(20) Kim, G. Y.; Oh, S. H.; Nguyen, B. P.; Jo, W.; Kim, B. J.; Lee, D. G.; Jung, H. S. Efficient Carrier Separation and Intriguing Switching of Bound Charges in Inorganic-Organic Lead Halide Solar Cells. *J. Phys. Chem. Lett.* **2015**, *6*, 2355−2362.

(21) Ning, Z.; Gong, X.; Comin, R.; Walters, G.; Fan, F.; Voznyy, O.; Yassitepe, E.; Buin, A.; Hoogland, S.; Sargent, E. H. Quantum-Dot-In-Perovskite Solids. *Nature* **2015**, *523*, 324−328.

(22) Butler, K. T.; Kumagai, Y.; Oba, F.; Walsh, A. Screening Procedure for Structurally and Electronically Matched Contact Layers for High-Performance Solar Cells: Hybrid Perovskites. *J. Mater. Chem. C* **2016**, *4*, 1149−1158.

(23) Kohn, W.; Sham, L. J. Self-Consistent Equations Including Exchange and Correlation Effects. *Phys. Rev.* **1965**, *140*, A1133−A1138.

(24) Kresse, G.; Joubert, D. From Ultrasoft Pseudopotentials to the Projector Augmented-Wave Method. *Phys. Rev. B: Condens. Matter Mater. Phys.* **1999**, *59*, 1758−1775.

(25) Blöchl, P. E. Projector Augmented-Wave Method. *Phys. Rev. B: Condens. Matter Mater. Phys.* **1994**, *50*, 17953−17979.

(26) Kresse, G.; Furthmüller, J. Efficient Iterative Schemes for *Ab Initio* Total-Energy Calculations Using a Plane-Wave Basis Set. *Phys. Rev. B: Condens. Matter Mater. Phys.* **1996**, *54*, 11169−11186.

(27) Kresse, G.; Furthmüller, J. Efficiency of *Ab-Initio* Total Energy Calculations for Metals and Semiconductors Using a Plane-Wave Basis Set. *Comput. Mater. Sci.* **1996**, *6*, 15−50.

(28) Perdew, J. P.; Ruzsinszky, A.; Csonka, G. I.; Vydrov, O. a.; Scuseria, G. E.; Constantin, L. a.; Zhou, X.; Burke, K. Restoring the Density-Gradient Expansion for Exchange in Solids and Surfaces. *Phys. Rev. Lett.* **2008**, *100*, 136406.

(29) Heyd, J.; Scuseria, G. E.; Ernzerhof, M. Hybrid Functionals Based on a Screened Coulomb Potential. *J. Chem. Phys.* **2003**, *118*, 8207−8215.

(30) Krukau, A. V.; Vydrov, O. A.; Izmaylov, A. F.; Scuseria, G. E. Influence of the Exchange Screening Parameter on the Performance of Screened Hybrid Functionals. *J. Chem. Phys.* **2006**, *125*, 224106.

(31) Butler, K. T.; Hendon, C. H.; Walsh, A. Electronic Chemical Potentials of Porous Metal-Organic Frameworks. *J. Am. Chem. Soc.* **2014**, *136*, 2703−2706.

(32) Butler, K. T.; Buckeridge, J.; Catlow, C. R. A.; Walsh, A. Crystal Electron Binding Energy and Surface Work Function Control of Tin Dioxide. *Phys. Rev. B: Condens. Matter Mater. Phys.* **2014**, *89*, 115320.

(33) Skelton, J. M.; Parker, S. C.; Togo, A.; Tanaka, I.; Walsh, A. Thermal Physics of the Lead Chalcogenides PbS, PbSe, and PbTe From First Principles. *Phys. Rev. B: Condens. Matter Mater. Phys.* **2014**, *89*, 205203.

(34) Lang, L.; Yang, J.-H.; Liu, H.-R.; Xiang, H. J.; Gong, X.-G. First-Principles Study on the Electronic and Optical Properties of Cubic ABX_3 Halide Perovskites. *Phys. Lett. A* **2014**, *378*, 290−293.

(35) Birch, F. Finite Elastic Strain of Cubic Crystals. *Phys. Rev.* **1947**, *71*, 809−824.

(36) Heifets, E.; Eglitis, R. I.; Kotomin, E. a.; Maier, J.; Borstel, G. *Ab Initio* Modeling of Surface Structure for $SrTiO_3$ Perovskite Crystals. *Phys. Rev. B: Condens. Matter Mater. Phys.* **2001**, *64*, No. 10.1103/PhysRevB.64.235417, DOI: 10.1103/PhysRevB.64.235417.

(37) Eglitis, R. I. *Ab Initio* Hybrid DFT Calculations of $BaTiO_3$, $PbTiO_3$, $SrZrO_3$ and $PbZrO_3$ (111) Surfaces. *Appl. Surf. Sci.* **2015**, *358*, 556−562.

(38) O'Sullivan, M.; Hadermann, J.; Dyer, M. S.; Turner, S.; Alaria, J.; Manning, T. D.; Abakumov, A. M.; Claridge, J. B.; Rosseinsky, M. J.

Interface Control by Chemical and Dimensional Matching in an Oxide Heterostructure. *Nat. Chem.* **2016**, *8*, 347−353.

(39) Du, M.-H. Density Functional Calculations of Native Defects in $CH_3NH_3PbI_3$: Effects of Spin-Orbit Coupling and Self-Interaction Error. *J. Phys. Chem. Lett.* **2015**, *6*, 1461−1466.

(40) Kang, J.; Wang, L.-W. High Defect Tolerance in Lead Halide Perovskite CsPbBr 3. *J. Phys. Chem. Lett.* **2017**, *8*, 489−493.

(41) Little, E. J., Jr.; Jones, M. M. A Complete Table of Electronegativities. *J. Chem. Educ.* **1960**, *37*, 231.

(42) Schoolar, R. B.; Dixon, J. R. Optical Constants of Lead Sulfide in the Fundamental Absorption Edge Region. *Phys. Rev.* **1965**, *137*, A667−A670.

(43) Stoumpos, C. C.; Malliakas, C. D.; Peters, J. a.; Liu, Z.; Sebastian, M.; Im, J.; Chasapis, T. C.; Wibowo, A. C.; Chung, D. Y.; Freeman, A. J.; et al. Crystal Growth of the Perovskite Semiconductor $CsPbBr_3$: A New Material for High-Energy Radiation Detection. *Cryst. Growth Des.* **2013**, *13*, 2722−2727.

(44) Amat, A.; Mosconi, E.; Ronca, E.; Quarti, C.; Umari, P.; Nazeeruddin, M. K.; Grätzel, M.; De Angelis, F. Cation-Induced Band-Gap Tuning in Organohalide Perovskites: Interplay of Spin-Orbit Coupling and Octahedra Tilting. *Nano Lett.* **2014**, *14*, 3608−3616.

(45) Jung, Y.-K.; Lee, J.-H.; Walsh, A.; Soon, A. Influence of Rb/Cs Cation-Exchange on Inorganic Sn Halide Perovskites: From Chemical Structure to Physical Properties. *Chem. Mater.* **2017**, *29*, 3181−3188.

(46) Filip, M. R.; Eperon, G. E.; Snaith, H. J.; Giustino, F. Steric Engineering of Metal-Halide Perovskites With Tunable Optical Band Gaps. *Nat. Commun.* **2014**, *5*, 5757.

(47) Yang, R. X.; Butler, K. T.; Walsh, A. Assessment of Hybrid Organic-Inorganic Antimony Sulfides for Earth-Abundant Photovoltaic Applications. *J. Phys. Chem. Lett.* **2015**, *6*, 5009−5014.

DOI: 10.1021/acs.jpcc.7b10000
J. Phys. Chem. C 2017, 121, 27351−27356